Applied Catalysis B: Environmental 240 (2019) 122–131

Contents lists available at ScienceDirect

Applied Catalysis B: Environmental

journal homepage: www.elsevier.com/locate/apcatb

Protonated g-C_3N_4/Ti^{3+} self-doped TiO_2 nanocomposite films: Room-temperature preparation, hydrophilicity, and application for photocatalytic NO_x removal

Yu Huang[a,b,*], Pengge Wang[a], Zhenyu Wang[a], Yongfang Rao[c], Jun-ji Cao[a,b], Shengyan Pu[d], Wingkei Ho[e], Shun Cheng Lee[f]

[a] State Key Lab of Loess and Quaternary Geology (SKLLQG), Institute of Earth Environment, Chinese Academy of Sciences, Xi'an, 710061, China
[b] Key Laboratory of Aerosol Chemistry and Physics, Institute of Earth Environment, Chinese Academy of Sciences, Xi'an, 710061, China
[c] Department of Environmental Science and Engineering, Xi'an Jiaotong University, Xi'an, 710049, China
[d] State Key Laboratory of Geohazard Prevention and Geoenvironment Protection, Chengdu University of Technology, Chengdu, 610059, China
[e] Department of Science and Environmental Studies, The Education University of Hong Kong, Hong Kong, China
[f] Department of Civil and Environmental Engineering, The Hong Kong Polytechnic University, Hong Kong, China

ARTICLE INFO

Keywords:
pCN/TiO_2films
Room-temperature preparation
Hydrophilicity
NO_x removal
Biocompatibility

ABSTRACT

Fabrication of photocatalysis films with good adhesion, hydrophilicity, and high activity on substrates at room temperature is essential for their application in air pollution control. Herein, functionalized transparent composite films containing ultrathin protonated g-C_3N_4 (pCN) nanosheets and Ti^{3+} self-doped TiO_2 nanoparticles (pCN/TiO_2) were fabricated on glass at room temperature. Thickness of the films measures 80 nm with surface roughness of 7.16 nm. The adhesion ability was attributed to the viscosity of TiO_2 sol, which served as "chemical glue" in the films. The high photo-induced hydrophilicity demonstrated their self-cleaning potential. pCN/TiO_2 films showed remarkably high visible-light-driven activity in terms of NO removal in a continuous-flow mode. Photoelectrochemical tests demonstrated the superior charge separation efficiency of pCN/TiO_2 films compared with that of pristine TiO_2. As identified by electron spin resonance spectra, $^{\cdot}O_2^-$ and $^{\cdot}OH$ radicals were the key reactive species involved in NO removal. The possible mechanism for photocatalytic NO oxidation was proposed. Potential cytotoxicity of pCN/TiO_2 films was evaluated by 3-(4,5-dimethylthiazol-2-yl)-2,5-diphenyltetrazolium bromide assay to ensure the biosecurity. This work provides a facile route to fabricate nanocomposite films under ambient temperature. The nanocomposite films were characterized by photo-induced hydrophilicity, high NO removal efficiency, and good biocompatibility, showing its potential in large-scale application.

1. Introduction

Air pollution has attracted increasing concerns regarding its potential adverse effects on air quality and human health [1,2]. The concentration of nitrogen oxides (NO_x) which contributes to the formation of secondary aerosols during haze episodes [3], substantially increased in the atmosphere over the past decades. However, deNO_x strategies, such as selective catalytic reduction and adsorption, are not technically suitable for ambient air purification [4–6]. Photocatalysis technology, a sustainable alternative for NO_x elimination at parts-per-billion (ppb) levels, demonstrates high efficiency on air pollutant removal through photo-induced reactive species [7–12].

Titanium dioxide has been widely used in energy conversion and environment remediation because of its abundance, stability, and excellent photocatalytic activity [13–15]. However, photocatalysts in powder form are not suitable for practical application in air pollution control because they are difficult to load or recycle, and may pose adverse effects on human health when ingested [16,17]. Phase composition of titanium dioxide nanoparticles strongly correlates with their cytotoxicity [18]. Therefore, it is essential for practical application and human health to fabricate photocatalytic films with good adhesive ability to avoid nanoparticles release into the environment. Sol-gel method, which exhibits high compatibility, is widely adopted to prepare titanium dioxide films on various substrates [19–21]. Glass substrates are extensively utilized in air purification [22,23], water decontamination [24,25], antimicrobial applications [26,27], and self-

* Corresponding author at: State Key Lab of Loess and Quaternary Geology (SKLLQG), Institute of Earth Environment, Chinese Academy of Sciences, Xi'an, 710061, China.
E-mail address: huangyu@ieecas.cn (Y. Huang).

https://doi.org/10.1016/j.apcatb.2018.08.078
Received 20 June 2018; Received in revised form 18 August 2018; Accepted 29 August 2018
Available online 01 September 2018

cleaning processes [28–30] because of their good light transmittance and easy cleaning properties. However, the preparation of titanium dioxide films using traditional sol-gel method requires high-temperature annealing to obtain superior crystallinity and reliable adhesion, remarkably limiting large-scale manufacture. High-temperature processing possesses detrimental effects on photoactivity and mechanistic property of substrates, such as sodium introduction and surface area reduction [31,32]. Therefore, the fabrication of titanium dioxide films with high adhesion ability at room temperature and excellent photoactivity is highly desirable but still poses a challenge.

Crystallinity of titanium dioxide significantly affects its photocatalytic activity. Apart from the high temperature/pressure procedures, peptization played a key role in facilitating the crystallization of titanium dioxide [33–36]. By controlling the peptizing parameters in a sol-gel progress, such as reaction temperature, acid addition, and aging time, the low-temperature driven titanium dioxide colloids with crystallization can be obtained [33,36]. Given its wide band gap of 3.2 eV, titanium dioxide is only sensitive to UV light, accounting for only 5% of the total solar energy [13]. Instead of introducing any impurities, an enough concentration of Ti^{3+} doping can extend the visible-light absorption range of titanium dioxide by introducing a localized state (0.75–1.18 eV) below the conduction band (CB) minimum, leading to the enhancement of visible-light-driven photocatalytic activity [37–41]. A low-activation energy drived low-temperature phase transformation in a sol-gel method was investigated by introducing an intermediate titanium hydroxylate, $Ti(OH)_x^{(3-x)+}$ [36]. Inspired by this approach, it is possible to prepare Ti^{3+}-doped titanium dioxide colloids at low-temperature.

Another way to improve the photocatalytic activity of titanium dioxide-based materials is coupling them with narrow band gap semiconductors, which has been proven effective in extending light response spectrum and relatively facilitating electron-hole pair separation [42]. As a metal-free and visible-light-driven (~470 nm) polymer, g-C_3N_4 attracts increasing attention due to its earth abundance, facile synthesis, physicochemical stability, and good biocompatibility [43–45]. The matched energy band and the biocompatible property make g-C_3N_4 a satisfactory alternative for maximizing the performance of titanium dioxide [46–48]. Unfortunately, g-C_3N_4 is usually in solid-state, hardly touched, and difficult to be directly immobilized on substrates, resulting in an actually limited application. Zhang and coworkers had firstly investigated a colloidal suspension of protonated g-C_3N_4 by concentrated HNO_3 refluxing at 80 °C, and fabricated the protonated g-C_3N_4 films on glass by annealing at 350 °C [49]. The protonated g-C_3N_4 can provide a better solubility/dispersability, which is favorable for its dispersion in solutions to form films. Besides, protonation can also adjust electronic band gap and improve charge separation efficiency of g-C_3N_4, enhancing photocatalytic activity [50,51]. Therefore, employing titanium dioxide sol as “chemical glue” and the advantages of protonated g-C_3N_4 to design visible-light-driven photocatalytic films is a promising strategy for air pollution control.

In this work, we proposed a facile method to fabricate protonated g-C_3N_4/Ti^{3+} self-doped titanium dioxide nanocomposite films (pCN/TiO_2) on glass substrate at room temperature. The films with good adhesion can be used for photocatalytic elimination of NO at ambient concentration (ppb) levels. Intrinsic properties of the as-prepared thin films were examined in detail. The mechanisms underlying NO removal and photocatalytic activity enhancement were discussed. 3-(4, 5-dimethylthiazol-2-yl)-2, 5-diphenyltetrazolium bromide (MTT) assay was performed for in vitro cytotoxicity assessment of pCN/TiO_2 films to ensure the biosecurity. To the best of our knowledge, this study is the first to prepare pCN/TiO_2 nanocomposite films at ambient temperature for air pollution control.

2. Experimental section

2.1. Preparation of pCN/TiO_2 composite films at room temperature

For the preparation of pCN/TiO_2 nanocomposite films, the sol composed of pCN nanosheets suspension and TiO_2 nanoparticles was first prepared. TiO_2 sol was prepared at room temperature according to a modified sol-gel method. In brief, tetrabutyl titanate (TBT) was added dropwise into 0.1 mol/L of HCl aqueous solution (volume ratio of 1:10) in an ice bath. It was vigorously stirred until the white precipitate was completely dissolved. Subsequently, the transparent solution was stored in a brown glass container at 25 °C for 14 days to crystallize. The amount of TiO_2 in the sol was determined to be 0.015 g/mL. Well-dispersed pCN suspension was obtained through ultrasonic exfoliation of pCN powder as details: firstly, g-C_3N_4 powder was prepared by a traditional method as displayed in supporting information; secondly, 1.0 g g-C_3N_4 and 10.0 mL HCl (37%) were mixed and stirring at room temperature for 12 h, subjected to centrifugal washing until the suspension was neutral, then dried overnight at 80 °C; thirdly, 0.01 g white pCN powder was ultrasonically exfoliated (150 W, 40 KHz) in 100 mL alcohol for 4 h to obtain a homogeneous solution.

pCN/TiO_2 films were prepared by spray-coating a series of ultrasonically treated mixture of TiO_2 sol and pCN suspensions for 5 times at volume ratios of 1:1, 1:2, 1:5, and 1:10 onto glass substrates at room temperature without further heat treatment, and the samples were denoted as T/C-1/1, T/C-1/2, T/C-1/5, and T/C-1/10, respectively. The mass ratios of pCN in these films were estimated to be 0.66%, 1.32%, 3.23%, and 6.25%, respectively. For comparison, pristine TiO_2 films were prepared by diluting TiO_2 sol with an equal volume of alcohol under identical conditions.

2.2. Characterization

Surface charges of g-C_3N_4 and pCN in ultrapure water were measured on a zeta potential analyzer (NanoBrook 90Plus PALS, Brookhaven, USA). X-ray diffraction (XRD, PAN analytical, X’pert, the Netherlands) was performed by recording Cu Kα radiation (λ = 1.5406 Å, 40 kV, 40 mA) at a scan rate of 0.04° 2θ/s to examine crystallographic properties. A Fourier-transform infrared spectroscopy (FTIR) absorption spectrometer (Magna-IR 750, Nicolet, USA) was used to analyze chemical composition and construction of samples using KBr as diluent. Characterizations of X-ray photoelectron spectra (XPS, Thermo ESCALAB 250, USA) were carried out on an X-ray photoelectron spectrometer. Elemental analyses were conducted on an Elementar Vario EL instrument (Vario EL III, Germany) with a detection limit of 0.015% and standard deviation of less than 0.1%. Adhesion of films coated on glasses was assessed based on the ISO 2409: 2013 method [52]. Absorption spectra and light transmittance were measured through a UV–vis diffuse reflection spectral system (DRS, Varian Cary 100 Scan UV–vis, USA) over a range of 200–800 nm using $BaSO_4$ as reference. Contact angle (CA, θ) was measured according to ISO 15989: 2004 [53] on a CA goniometer system (SL200KS, KINO Industry, USA). Surface morphologies and film thickness were observed through scanning electron microscopy (SEM, JEOL JSM-6490, Japan). Highly defined images of morphological structures of the samples were obtained through transmission electron microscopy (TEM, JEM-2010, Japan). Film surface roughness was measured through atomic force microscopy (AFM, Dimension Icon, Bruker, Germany). The photocatalytic NO oxidation products remaining in the films after the photocatalytic activity test were analyzed by immersing the films into 50 mL ultrapure water for 30 min and then subjected to ion chromatpgraphy using a Dionex-600 Ion Chromatograph (IC, Dionex Inc., Sunnyvale, CA, USA) equipped with an IonPac AS14 A column. Reactive radical formation was detected through electron spin resonance spectroscopy (ESR, ER200-SRC, Bruker, Germany) using 5, 5-dimethyl-1-pyrroline-*N*-oxide (DMPO) as spin-trap reagent under visible light irradiation. 0.05 g

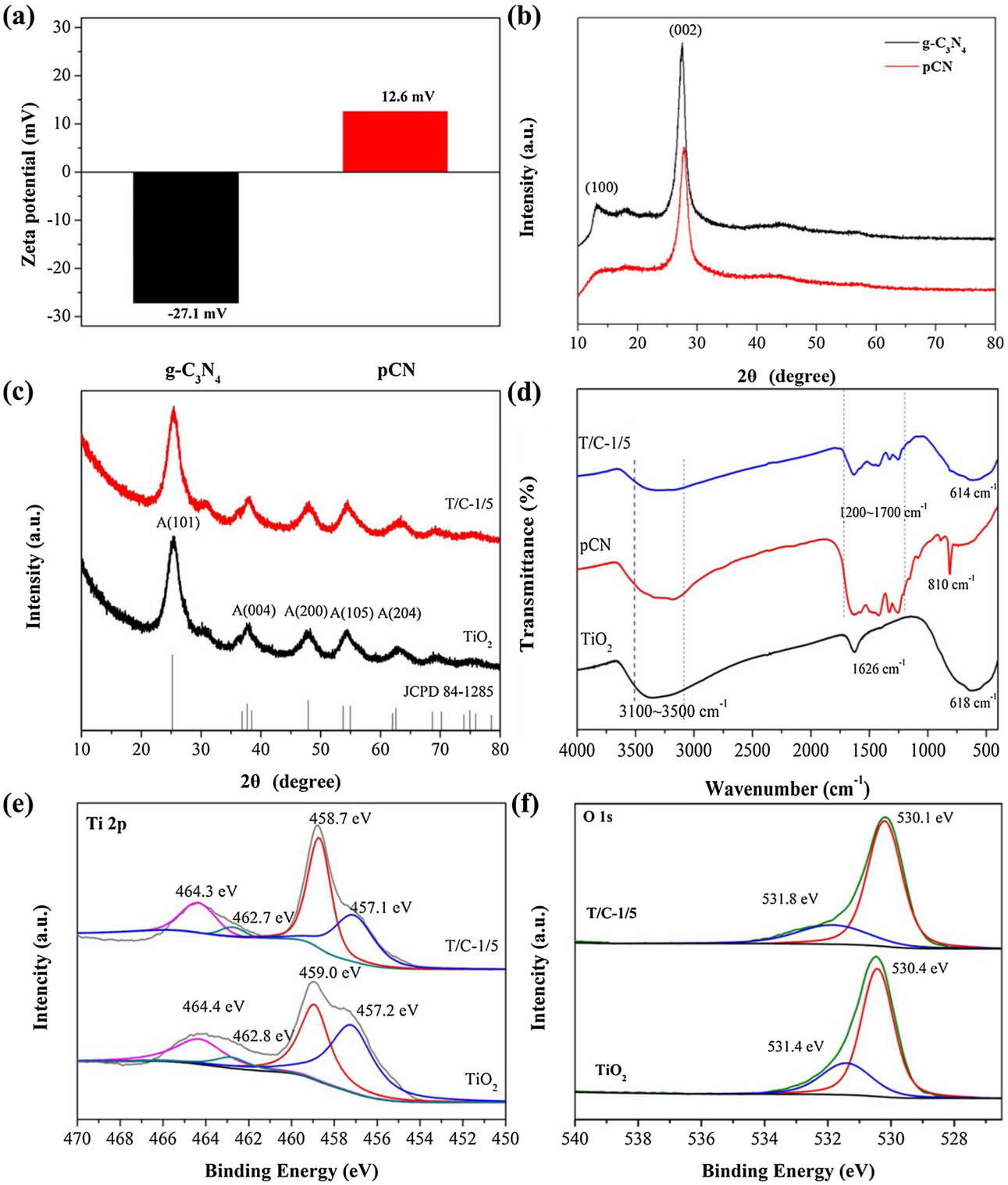

Fig. 1. Zeta potential (a) and XRD (b) of g-C_3N_4 and pCN; XRD patterns of TiO_2 and T/C-1/5 films (c); FT-IR spectra of TiO_2, pCN and T/C-1/5 films (d); high-resolution XPS spectra of Ti 2p (e) and O1s (f) of TiO_2, and T/C-1/5 films.

sample was dispersed into 25 mM DMPO solution with a 50 mL aqueous dispersion for DMPO-˙OH or 50 mL methanol dispersion for DMPO-$˙O_2^-$, respectively. A 300 W Xe arc lamp (PLS-SXE 300, Beijing) with a UV cutoff filter (λ > 420 nm) was used as visible light source.

Photocatalytic activity measurement, photoelectrochemical measurement and cytotoxicity assay were detailed in supporting information.

3. Results and discussion

3.1. Crystal structure and chemical composition

As shown in Fig. 1a, the zeta potential value of g-C_3N_4 dispersed in deionized water increased from −27.1 mV to + 12.6 mV after HCl tuning, proving successful protonation [51]. XRD patterns showed two characteristic peaks at 13.1° and 27.6° indexed as (100) and (002)

crystal planes of g-C_3N_4 (JCPDS 87-1526) (Fig. 1b). The peak vanishing at 13.1° of pCN was mainly caused by destruction of the in-plane periodic tri-s-triazine units, and the retained (002) peak indicated a well-maintained interlayer stacking of the conjugated aromatic system of g-C_3N_4, suggesting the expected effective exfoliation of bulk g-C_3N_4 [50,54,55].

A well-crystallized TiO_2 indexed to the tetragonal anatase phase was obtained (JCPD 84-1285) (Fig. 1c). This result suggests that without high-temperature processing, crystallized TiO_2 can still be fabricated through real-time in situ crystallization of TiO_2 sol during peptization in acidic conditions [33,36]. Typical diffraction peaks of g-C_3N_4 were not evident in the composite probably because of low loading amount. FTIR analysis was carried out to verify the presence of pCN (Fig. 1d). Notably, absorption peaks centered at 1254, 1328, 1416, 1490, 1578, and 1629 cm^{-1} in the range of 1200–1700 cm^{-1}, were corresponded to typical CN heterocycles [56]. Another wide peak appearing at 400–700 cm^{-1} can be assigned to Ti—O stretching and Ti—O—Ti bridge stretching modes [42]. These characterization results indicated successful modification of TiO_2 by pCN.

Elemental analysis was employed to quantify chemical components (Table S1). Both C/N ratio and total C and N contents of g-C_3N_4 samples changed after protonation. C/N molar ratio of pCN reached 0.55, which was lower than that of g-C_3N_4 (0.59); C and N total mass contents decreased from 98.81% to 86.45%. Variation in chemical constitution and structure of g-C_3N_4 can be ascribed to the increase in exposed amine groups [50].

As shown in Fig. S2a, XPS spectra indicated the presence of C, N, Ti, and O in T/C-1/5 films. Given the remarkably low content of pCN in the composite, signals of C and N atoms were considerably weak. High-resolution Ti 2p spectra of TiO_2 (Fig. 1e) showed that the two distinct highly symmetric peaks at approximately 459.0 and 464.4 eV can be assigned to Ti $2p_{3/2}$ and Ti $2p_{1/2}$ of Ti^{4+} in TiO_2, respectively [40]. Notably, two shoulder peaks of 457.2 and 462.8 eV were confirmed to be $2p_{3/2}$ and $2p_{1/2}$ core levels of Ti^{3+} [57], respectively. A semi-quantitative analysis of the content of Ti^{3+} in the surface of TiO_2 calculated based on the high-resolution Ti 2p spectra was approximately 16.16%, the detailed calculation was displayed in supporting information. The remarkable presence of Ti^{3+} may be attributed to the intermediate titanium hydroxylate, $Ti(OH)_x^{(3-x)+}$, which played as a springboard in the phase transformation at low temperature as reported in previous study [36]. The presence of the large amount of Ti^{3+} is effective to enhance visible-light absorption of TiO_2 by creating donor states below the conduction band [37,38,58]. In O1s high-resolution spectrum, two evident peaks appeared at 530.4 and 531.4 eV in TiO_2, corresponding to the Ti—O and H—O bonds, respectively (Fig. 1f). Compared with that in pristine TiO_2, distinct variation of binding energy in T/C-1/5 films suggested changes in inner electron density of pCN and TiO_2, indicating successful pCN modification on TiO_2.

3.2. Optical absorption and photo-induced hydrophilic properties

The films were uniformly coated on glasses (Fig. 2a and inset) and exhibited excellent light transmittance of 90% (Fig. 2b). According to the ISO method, the adhesion ability of samples can be classified as 0 grade, which is the highest grade in the standard (Fig. S3, Table S2). It was employed as chemical glue; the TiO_2 sol had a significant effect on pCN immobilization. Different ratios of TiO_2 and pCN resulted in different loading amount of the composite films. When the ratio of pCN increased sharply, the adhesive of TiO_2 was limited, leading to a lower content of the films, as displayed in Table 1.

As described in Fig. S4, TiO_2 sol underwent hydrolysis/condensation and peptization can be stable over several weeks [35,59]. Herein, a probable mechanism about low-activation energy derived low-temperature reaction was proposed. As has been reported previously, the sol-gel method is a reliable way to synthesize ultra-fine TiO_2 nanocrystals through hydrolysis and condensation of titanium alkoxides in aqueous media at low temperature (< 100 °C) [33,60]. At high water-to-titanium mole ratio, a large excess of water can hydrolyze titanium alkoxide fastly, the processes of nucleation, growth, and aggregate were rapidly, leading to a white unstable suspension immediately [35]. H^+ could form complexes with metallic ions, slowing down the condensation reaction in a more orderly manner, and producing crystalline TiO_2 [61]. Generally, crystallization is occurred by rearrangement of the gel structure as reaction of alkoxide and hydroxide groups located on the surface of the hydrated TiO_2 particles during drying with sufficient thermal energy. While, aging process can change physical properties of the sol by polymerization, coarsening and phase transformation [62]. Thus, in the presence of acid aqueous solution, a low-activation energy promoted bond dissociation and reformation by aging process was involved, leading to a formation of TiO_2 nanocrystals when dried at room temperature. Besides, the adhesion of TiO_2 sol on glass substrates at room temperature can be explained. Several silicon-oxygen bonds and hydroxyl groups in glass and colloid TiO_2 with portions of alkoxy and hydroxyl groups can form firm Ti—O—Si and hydrogen bonds on the glass surface, contributing to strong adhesive ability.

Optical response of the samples was investigated by UV–vis DRS, as shown in Fig. 2c. Absorption edge of pristine TiO_2 appeared at approximately 421 nm, and the energy gap was calculated to be 2.94 eV (inset in Fig. 2c). The significant redshift was considered as Ti^{3+} self-doping [40,41], as discussed in XPS. Besides modifying dispersability, pronation process also changed the electronic structure of g-C_3N_4. Absorption edge of pCN appeared at approximately 440 nm, demonstrating a blue shift in comparison with that of g-C_3N_4. This observation should be attributed to the weakening of the π-conjugated system of g-C_3N_4 through reduced condensation [63]. Compared with pristine TiO_2, pCN/TiO_2 composites displayed more light absorption in the visible zone to some extent. The increase in pCN contents strengthened the redshift in the range of 421–440 nm because of the visible-light-harvesting property of pCN.

An enhanced absorption in the visible spectral range also allows a larger self-cleaning potential for outdoor application. Theoretically, when photocatalytic materials are exposed to light with sufficient energy, photo-excited electrons (e^-) and holes (h^+) are produced; minority of them react with atmospheric oxygen and surface-adsorbed water to generate superoxide radicals ($\cdot O_2^-$) and hydroxyl radicals ($\cdot OH$). Further, these reactive oxide species can efficiently convert most organic pollutants into inorganic products, resulting in a clean surface. Beyond that, a hydrophilic surface was also induced by illumination. When water droplets spread over the surface, the contaminants are easily washed away [30]. The self-cleaning potential of the as-prepared films was evaluated by measuring CA values over the coating surface after Xe lamp irradiation for 3 min [64]. Evidently, CA values of the TiO_2 and T/C-1/5 films decreased sharply from 27.1° and 39.1° to 8.1° and 6.4° (Fig. 2d), respectively, indicating that the surface of photocatalytic films became hydrophilic, whereas no significant difference was observed between CA values of blank glass before (CA = 30.4°) and after (CA = 28.9°) the same process. Although the adding of pCN leads to a larger CA value compared with that of pristine TiO_2 before irradiation, the final CA value of the composite was smaller, which may be caused by a higher light utilization efficiency of pCN. Numerous investigations proposed mechanisms underlying the photo-induced hydrophilicity of TiO_2-based materials, among which the theory proposed by Wang et al. was widely accepted [65]. In this mode, surface oxygen vacancies caused by diffusion of photo-generated holes play major roles. Ti^{4+} is reduced to Ti^{3+}, dissociating water molecules and facilitating the adsorption of −OH species on surfaces. The satisfactory photoinduced hydrophilicity of the films showed their brilliant prospect in application. When the films are used outside, rainwater is expected to be useful to keep the surface out of dirty, which is of great significance for NO_x removal.

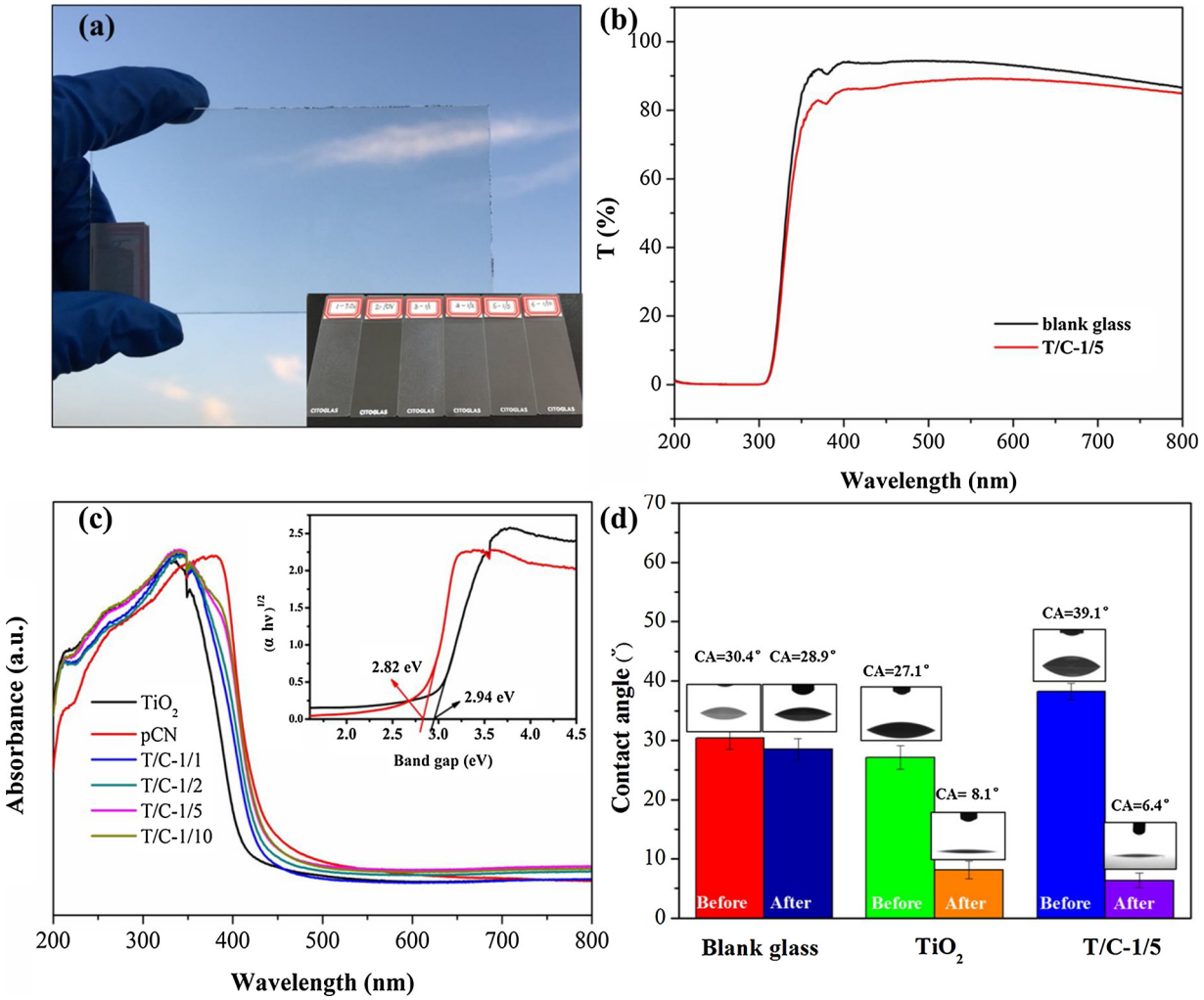

Fig. 2. Optical photograph of pCN/TiO_2 films (a); light transmittance of blank glass and T/C-1/5 films (b); UV–vis absorption spectra (inset: plots of $(\alpha h\nu)^{1/2}$ versus the photo energy of as-synthesized samples (c); CA variation of blank glass, TiO_2 and T/C-1/5 films before and after 3 min exposure to solar light (d).

Table 1
The loading mass for TiO_2, pCN, and pCN/TiO_2 films various ratios.

samples	TiO_2	pCN	T/C-1/1	T/C-1/2	T/C-1/5	T/C-1/10
Δm g/m^2	6.15	0.42	4.05	7.46	6.08	3.47

3.3. Morphologies

As shown in Fig. 3a, SEM images indicated that the glass surface was covered with heterogeneous nanosized particles and sheets. T/C-1/5 films consisted of grain-like TiO_2 nanoparticles and feather-shaped pCN nanosheets. Thickness of the films measured ~80 nm (Fig. 3b). Although impurities were present in TiO_2 sol, small TiO_2 aggregates of about 20 nm in width and ~50 nm in length, with crystallization were observed (Fig. 3c). High-resolution TEM images in Fig. 3d displays a lattice fringe spacing of 0.23 nm, which can be ascribed to the (004) facet of tetragonal anatase TiO_2 (JCPD 84-1285), thus coinciding with XRD results. Considering the high surface energy of ultrathin g-C_3N_4 nanosheets, being closely covered by TiO_2 nanoparticles can contribute to the decreased surface energy, increased charge mobility and reduced recombination rates. Surface topography and roughness of T/C-1/5 films were determined by AFM, as shown in Fig. 3e and f. In large-scale view (5 μm × 5 μm), the 2D image exhibited granular microstructure consisting of nanosized grains; this finding was in accordance with SEM results. 3D angle views of the films presented a sharp hill-valley surface with 7.16 nm roughness. These dense valley structures may extend contact time of air flow, favoring photocatalytic effect of the films.

3.4. Photocatalytic activity, identification of reactive species, and reaction mechanism

Low-concentration (ppb level) NO removal was surveyed in a specialized air purification system with photocatalytic films under visible-light irradiation. (Fig. S1) As shown in Fig. S5, NO_x concentration remained unchanged without any samples under visible-light irradiation in the system, indicating the reliability of the evaluation system. During photocatalytic reaction, most samples exhibited visible-light activity without any inactivation in 30 min, as shown in Fig. 4a. The sharply decrease of NO concentration in the first 5 min can be fully explained by the Langmuir-Hinshelwood kinetics model, the initial photocatalytic degradation of NO was fitted well with the mass-transfer-controlled pseudo-first-order rate reaction [66,67]. NO removal ratio (C/C_0 %) of 13.4% was obtained over pure TiO_2 films through self-doping of Ti^{3+}, whereas approximately 3.0% was observed for pCN films. When the amount of pCN increased, NO removal ratio accreted and reached approximately 25.8% at 1/5 proportion of TiO_2 and pCN and markedly decreased to 15.8% at 1/10. Notably, after modification with pCN, NO concentration significantly decreased in 2 min and remained relatively stable. NO_2 byproduct yield was negligible during NO elimination over all the films (Fig. S6). Excellent photodegradation efficiency of NO and

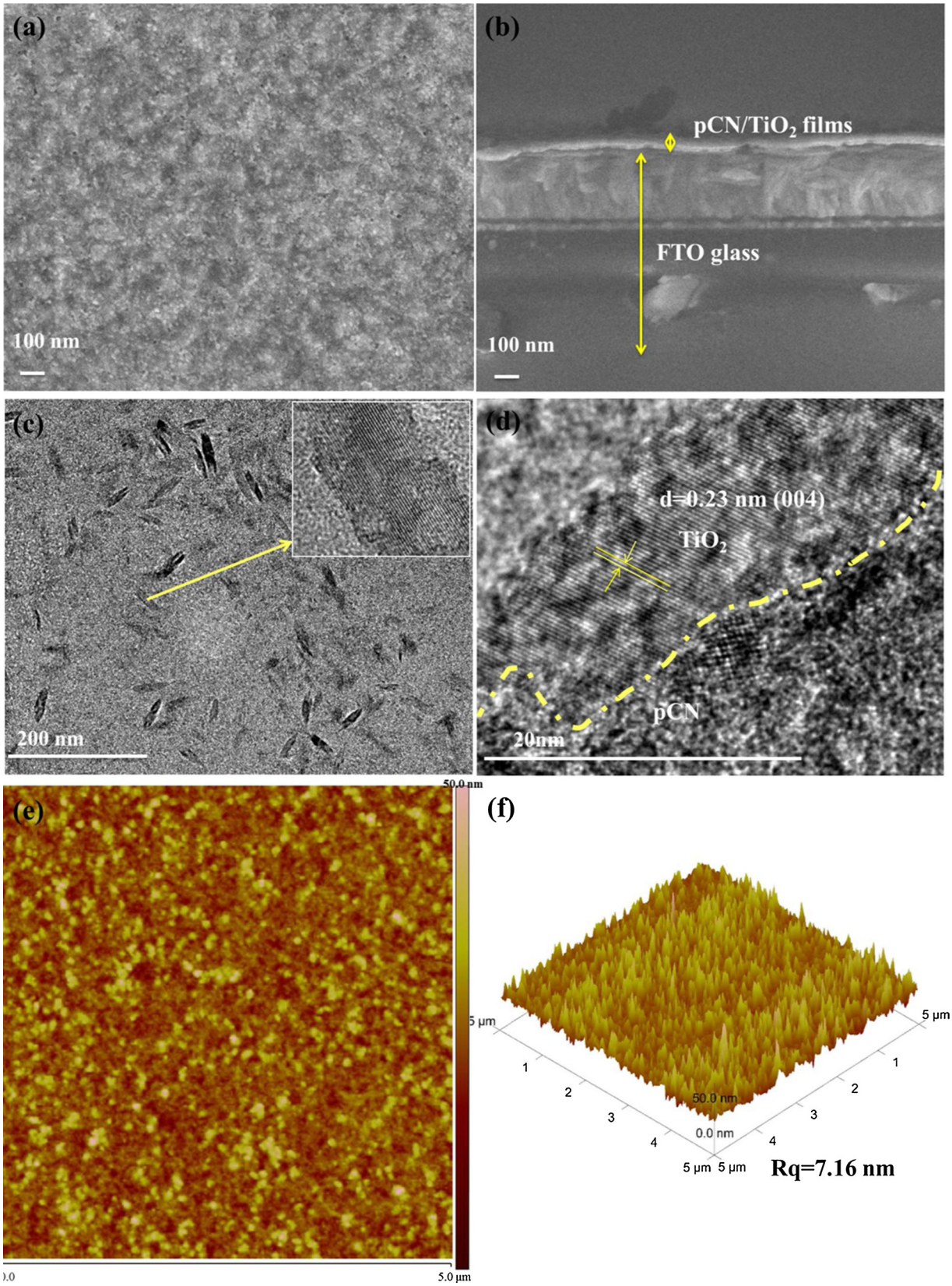

Fig. 3. Surface (a) and cross-sectional (b) SEM micrographs of T/C-1/5 films; low-magnificationand high-resolution TEM images of TiO_2 sol (c); high-resolution TEM images of T/C-1/5 films (d) ; 2D (e) and 3D (f) AFM images of T/C-1/5 films.

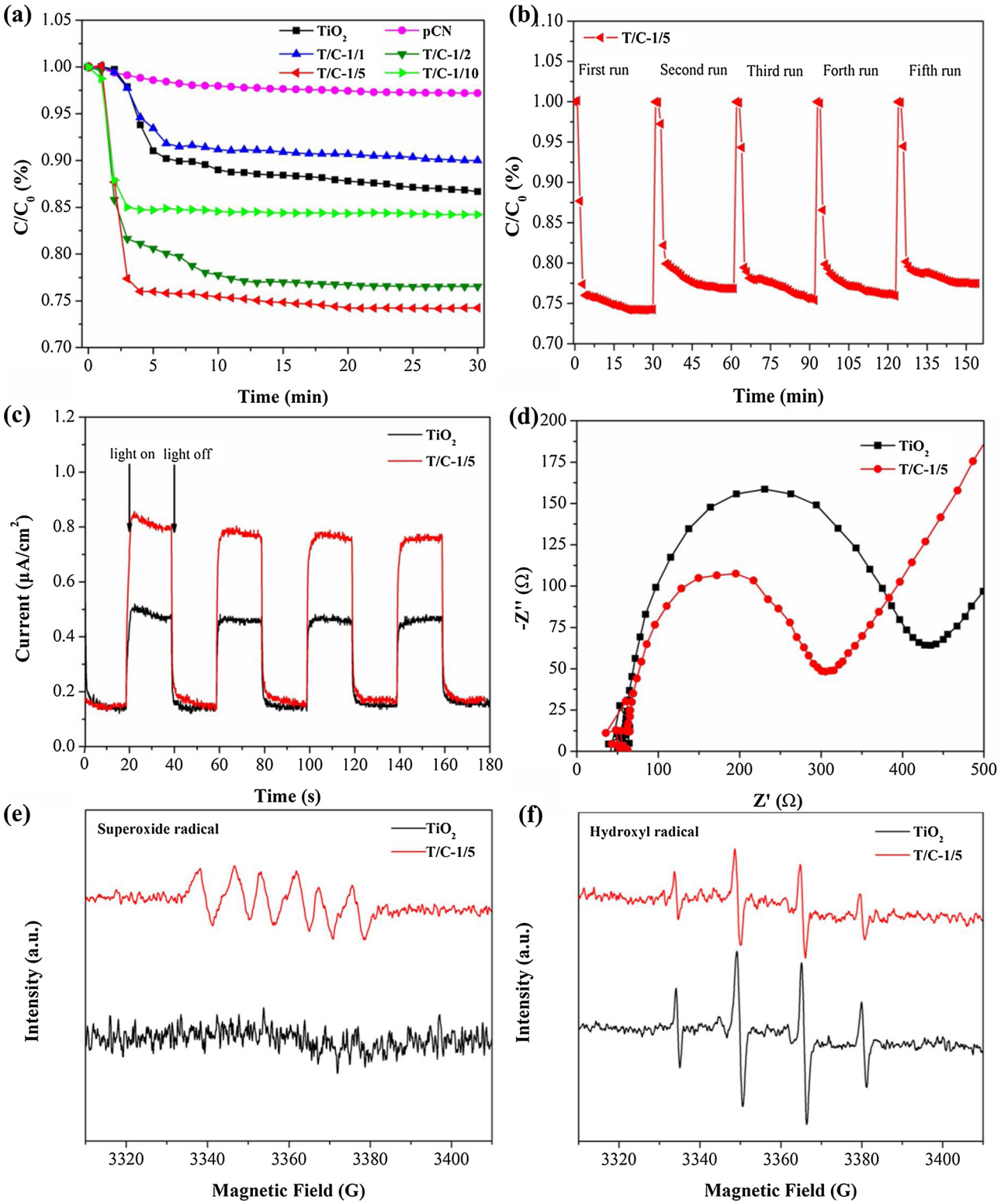

Fig. 4. Visible-light (λ > 420 nm) induced photocatalytic activities of the as-prepared films for NO removal (a) and cycling runs for photocatalytic removal of NO over T/C-1/5 films (b); photocurrent response (c) and Nyquist plots (d) of TiO_2 and T/C-1/5 electrodes under visible-light irradiation; DMPO spin-trapping ESR spectra of TiO_2 and T/C-1/5 in methanol dispersion for DMPO-$^{\cdot}O_2^-$ (e) and aqueous dispersion for DMPO-$^{\cdot}$OH (f).

satisfactory NO_2 selectivity of T/C-1/5 films can be attributed to the synergistic effects of pCN and Ti^{3+} self-doped TiO_2, which broadened the light response spectrum and promoted charge separation.

Fig. 4b showed that photocatalytic activity of the T/C-1/5 films was maintained after five runs with an insignificant decrease in stability. We supposed that the slight decrease could be ascribed to the accumulation of the photocatalytic NO oxidation products, which were verified through ion chromatography analysis (Table S3). The result suggested that nitrate (NO_3^-, 3.609 μg/m^2) and unstable intermediate nitrite (NO_2^-, 0.578 μg/m^2) were detected. To further test the stability of the films, the crystal structure, morphology, and the roughness of the films before and after the photocatalytic activity test were carried out by

XRD, SEM, and AFM as shown in Figs. S7-S9. As there were no obvious differences in the structure, morphology, and the roughness of the films, a long time photocatalytic NO removal test was conducted over T/C-1/5 films under visible light irradiation for 5 h (Fig. S10), implying that the NO removal rate of the films was relative stable and the by-product of NO_2 was at low concentration during the test. Thus, although the accumulation of NO_3- and NO_2^- may occupy the reactive sites of the photocatalyst resulting in a minor adverse effect on the photocatalytic performance, the decrease in the stability of the films was accepted for practical application.

Loading amount of photocatalyst is another key factor for photocatalytic activity. With a certain volume of as-prepared composite sols, loading mass of the films differed distinctly. Given the low pCN loading on glasses due to the difficulty of pCN adherence to glass at ambient temperature (Table 1), the pCN films exhibited negligible activity. When appropriate amount of TiO_2 sol was employed as chemical glue, NO removal ratio remarkably increased with the enhancement of pCN loading mass. It should be noted that T/C-1/5 film exhibited much higher photocatalytic activity than TiO_2 did under visible light irradiation with similar amount of these two catalysts being loaded on glass.

The photocatalytic activity enhancement and mechanisms underlying NO removal were discussed. Fig. 4c shows the photocurrent density obtained on TiO_2 and T/C-1/5 films modified FTO electrodes. The photocurrent density obtained on T/C-1/5 electrode reached 0.85 $\mu A{\cdot}cm^{-2}$, which considerably exceeded that of pristine TiO_2 electrode (0.45 $\mu A{\cdot}cm^{-2}$), suggesting higher charge separation efficiency. This result was also supported by the Nyquist semicircle, in which a smaller diameter was obtained for T/C-1/5 electrode (Fig. 4d), indicating better conductivity for electron transfer.

The band edge positions of photocatalysts were theoretically calculated based on the Mulliken electronegativity theory [68], which was described as Eqs. (1) and (2),

$$E_{CB} = X - E_c - 0.5E_g \quad (1)$$

$$E_g = E_{VB} - E_{CB} \quad (2)$$

Where, E_{CB} and E_{VB} are the CB minimum and the VB maximum (*vs.* NHE), E_g means the band gap energy of the photocatalyst, E_c is the energy of free electrons (4.5 eV), and X ($X = (X_1X_2X_3....X_n)^{1/n}$) is the geometric mean of the Mulliken electronegativity of the constituent atoms in the semiconductor.

Subsequently, the VB and CB edges of a prototypical anatase TiO_2 (Eg = 3.2 eV) were determined to be 2.9 eV and −0.3 eV, respectively. Considering that the band gap of TiO_2 in this study narrowed at 2.94 eV, we hypothesized that the energy levels of Ti^{3+} states below the CB of TiO_2 was positive than the redox potential of $^{\cdot}O_2^-/O_2$ (−0.33 eV) [11]. Meanwhile, the band gap of pCN was 2.82 eV, E_{CB} and E_{VB} of pCN were determined to be -1.16 eV and 1.66 eV, respectively.

As displayed in Fig. 4e, no DMPO-$^{\cdot}O_2^-$ adduct signals were observed for TiO_2, whereas six visible signals were generated for T/C-1/5 and were attributed to the reduction of O_2 by photo-generated electrons of pCN. As shown in Fig. 4f, DMPO-$^{\cdot}$OH signals were detected over both TiO_2 and T/C-1/5 samples. The DMPO-$^{\cdot}$OH signals were stronger over TiO_2 than those over T/C-1/5. The photo-generated holes of pCN cannot oxidize H_2O/OH^- to $^{\cdot}$OH but can oxidize NO to nitrate. ($E(^{\cdot}OH/OH^-) = 1.99$ eV, $E(^{\cdot}OH/H_2O) = 2.73$ eV) [69]. Thus, the $^{\cdot}$OH species observed in T/C-1/5 system were generated by TiO_2. Meanwhile, the photo-generated holes of T/C-1/5 system transferred from the valance band (VB) of TiO_2 to that of pCN, resulting in a decrease in DMPO-$^{\cdot}$OH signals. These results indicate that pristine TiO_2 cannot generate $^{\cdot}O_2$- radicals under visible-light illumination. In the system of T/C composite, both $^{\cdot}$OH and $^{\cdot}O_2$- radicals performed concerted function on NO_x removal in the same condition.

The probable charge transfer mechanism was proposed in Fig. 5. The doping of Ti^{3+} can form new states at the bottom of the TiO_2 CB. Under visible-light irradiation, both Ti^{3+} self-doped TiO_2 and pCN in pCN/TiO_2 system generated photo-induced electron-hole pairs, which were spatially separated by migrating the charge carriers apart from each semiconductor. The VB and CB potentials of pCN are negative than that of TiO_2 and the Ti^{3+} states, respectively, allowing the holes of TiO_2 partly transfer to that of pCN, and the electrons of pCN transfer to the Ti^{3+} states. This process resulted in efficient space separation of photo-induced charge carriers to suppress recombination. The remaining holes in the VB of TiO_2 could directly oxidize NO to NO_3^-, and simultaneously react with H_2O/OH^- to produce $^{\cdot}$OH. Though Ti^{3+} doping broaden the range of visible absorption of TiO_2 due to the Ti^{3+} states, the reduction ability of electrons in Ti^{3+} states was low (−0.03 eV), which cannot reduce O_2 by one electron reduction (−0.046 eV) [70]. Otherwise, the electrons at the CB of pCN can absorb O_2 to generate $^{\cdot}O_2^-$. Both of the $^{\cdot}$OH and $^{\cdot}O_2^-$ with strong oxidation ability could completely oxidize NO to NO_3^-. The detailed reaction processes of photocatalytic NO removal by pCN/Ti^{3+} self-doped TiO_2 films are described as Eqs. (3)–(10).

$$TiO_2\ (Ti^{3+}) + h\nu \rightarrow e^-\ (TiO_2) + \mathbf{h}^+\ (TiO_2) \quad (3)$$

$$pCN + h\nu \rightarrow \mathbf{e}^-\ (pCN) + h^+\ (pCN) \quad (4)$$

$$\mathbf{h}^+\ (TiO_2) + H_2O/OH^- \rightarrow {}^{\cdot}OH \quad (5)$$

$$\mathbf{e}^-\ (pCN) + O_2 \rightarrow {}^{\cdot}O_2\text{-} \quad (6)$$

$$^{\cdot}OH + NO \rightarrow NO_3^- \quad (7)$$

$$^{\cdot}O_2^- + NO \rightarrow NO_3^- \quad (8)$$

$$\mathbf{h}^+\ (TiO_2) + NO \rightarrow NO_3^- \quad (9)$$

$$h^+\ (pCN) + NO \rightarrow NO_3^- \quad (10)$$

4. Cytotoxicity assessment

Possible cytotoxicity of photocatalytic materials is an important factor for evaluating their potential for practical application. Considering that inhalation is a major mode of intake, classical MTT assay was performed to investigate the cytotoxic effect of the as-prepared samples on human lung adenocarcinoma cells. Within a wide range of concentrations (0.5–100 μg/mL), T/C-1/5 composite was more compatible with A549 cells than pure TiO_2. As shown in Fig. 6a, a direct dose–response relationship was observed for the tested cells at high concentrations (5–100 μg/mL). Insignificant loss of cell viability was observed for T/C-1/5-incubated cells; this condition promoted cell proliferation at high concentration (100 μg/mL), indicating excellent biocompatibility and nontoxicity. In the case of control group, approximately 50% inhibition in cell viability was observed at TiO_2 concentration of 100 μg/mL. Cell imaging and in vitro cellular uptake of samples are demonstrated in Fig. 6b, 6c, and S11. A strong and bright green fluorescence emission under excitation at 488 nm was readily observed in A549 cells incubated with T/C-1/5. In the case of control group, almost no fluorescence signals were observed in TiO_2-incubated cells, and cell morphology showed remarkable variation (Fig. S11). This result suggested that the T/C-1/5 composite can be rapidly delivered into cells with perfect biocompatibility and minimum cytotoxicity, exhibiting its safety for application.

In summary, photocatalytic pCN/TiO_2 composite films were successfully fabricated at room temperature on glass substrates for air purification. Self-doping of TiO_2 with Ti^{3+} can modulate the electronic structure of TiO_2 by creating donor states below the CB minimum. The heterogeneous structure effectively enhanced the harvest of visible-light and charge separation efficiency. The obtained pCN/TiO_2 films exhibited a considerably high and stable photocatalytic activity (i.e., NO removal rate reached approximately 25% under visible-light), ideal transmittance, and photo-induced hydrophilicity for potential self-

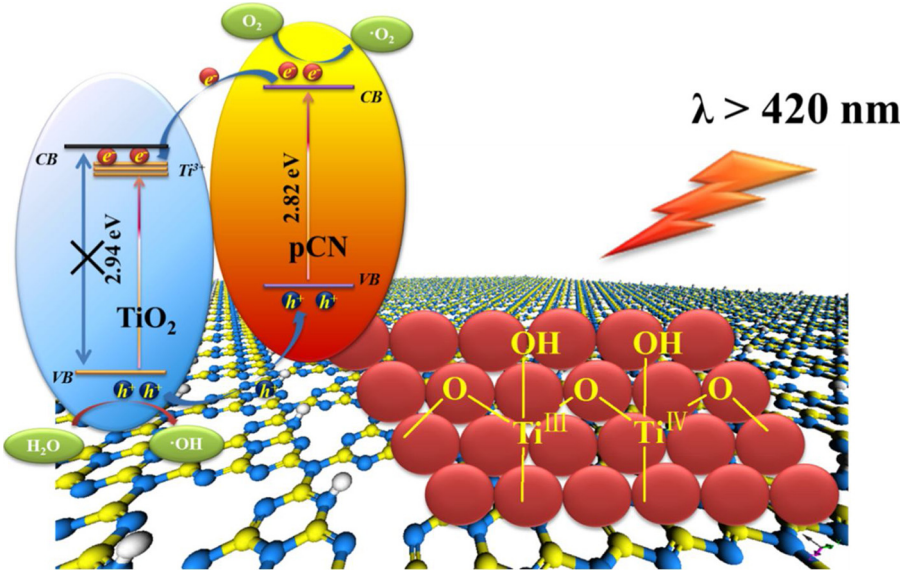

Fig. 5. Schematic illustration of the proposed mechanism for charge transfer and radical generation under visible-light irradiation.

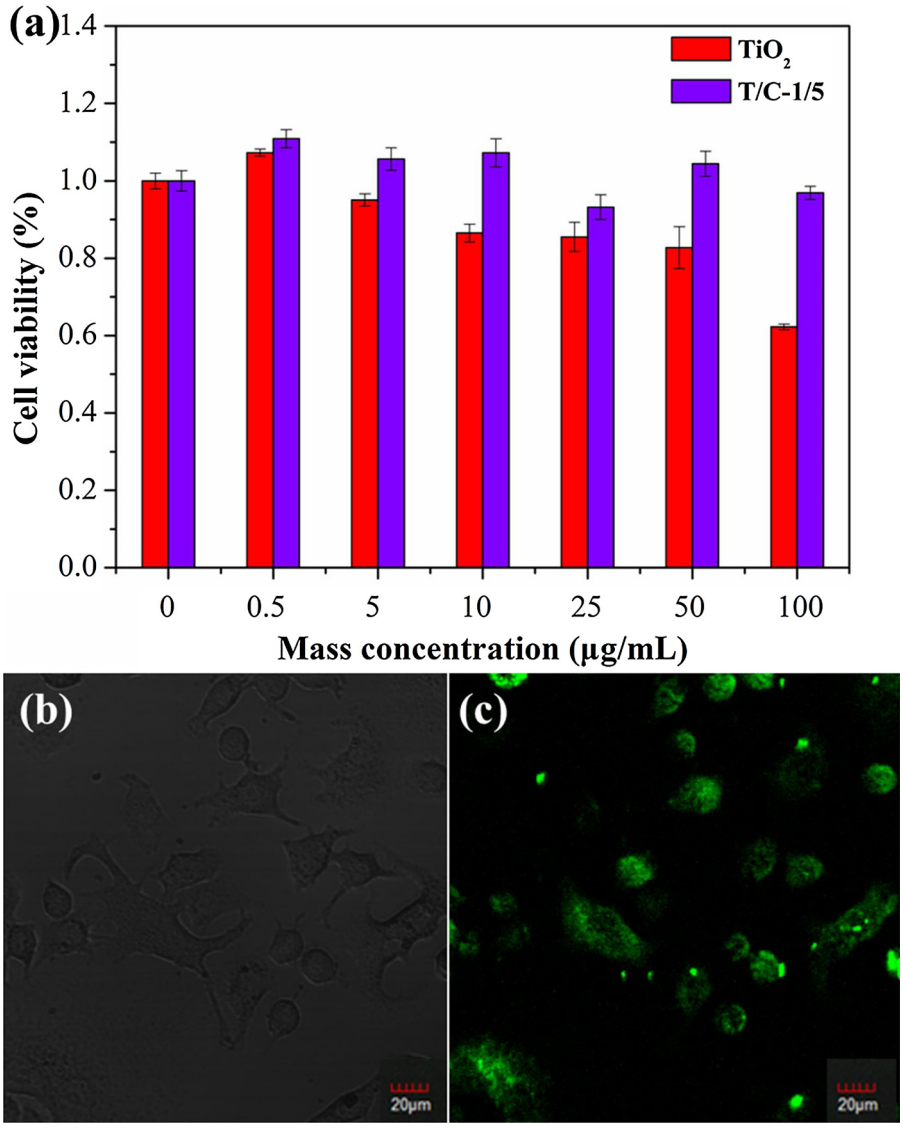

Fig. 6. Cell survival rate of A549 after exposure to different concentrations of TiO_2 and T/C-1/5 saline solution for 24 h (a); bright-field (b) and dark-field (c) images of A549 cells incubated with 50 μg/mL T/C-1/5 saline solution for 1 h.

cleaning application. Furthermore, the pCN/TiO_2 films are safe for use according to MTT assay results. The prepared films are promising for large-scale environmental applications.

Notes

The authors declare no competing financial interest.

Acknowledgments

This research was financially supported by the National Key Research and Development Program of China (2016YFA0203000), the State Key Lab of Loess and Quaternary Geology (SKLLQGPY1605), and the National Science Foundation of China (No. 41573138). This study was also partially supported by the Key Project of International Cooperation of the Chinese Academy of Sciences (GJHZ1543) and the Research Grants Council of Hong Kong (PolyU 152083/14E). Yu Huang is also supported by the "Hundred Talent Program" of the Chinese Academy of Sciences.

Appendix A. Supplementary data

Supplementary material related to this article can be found, in the online version, at doi:https://doi.org/10.1016/j.apcatb.2018.08.078.

References

[1] M. Gao, P.E. Saide, J. Xin, Y. Wang, Z. Liu, Y. Wang, Z. Wang, M. Pagowski, S.K. Guttikunda, G.R. Carmichael, Environ. Sci. Technol. 51 (2017) 2178–2185.
[2] R.-J. Huang, Y. Zhang, C. Bozzetti, K.-F. Ho, J.-J. Cao, Y. Han, K.R. Daellenbach, J.G. Slowik, S.M. Platt, F. Canonaco, Nature 514 (2014) 218–222.
[3] B. Zhao, S.X. Wang, H. Liu, J.Y. Xu, K. Fu, Z. Klimont, J.M. Hao, K.B. He, J. Cofala, M. Amann, Atmos. Chem. Phys. 13 (2013) 9869–9897.
[4] I. Heo, M.K. Kim, S. Sung, I.S. Nam, B.K. Cho, K.L. Olson, W. Li, Environ. Sci. Technol. 47 (2013) 3657–3664.
[5] W.S. Epling, L.E. Campbell, A. Yezerets, N.W. Currier, J.E. Parks, Catal. Rev. 46 (2004) 163–245.
[6] Q. Guo, T. Sun, Y. Wang, Y. He, J. Jia, Environ. Sci. Technol. 47 (2013) 9514–9522.
[7] Y. Huang, Y. Liang, Y. Rao, D. Zhu, J.J. Cao, Z. Shen, W.K. Ho, S.C. Lee, Environ. Sci. Technol. 51 (2017) 2924–2933.
[8] Y. Lu, Y. Huang, Y. Zhang, J.J. Cao, H. Li, C. Bian, S.C. Lee, Appl. Catal. B: Environ. 231 (2018) 357–367.
[9] Z. Wang, Y. Huang, W.K. Ho, J.-J. Cao, Z.X. Shen, S.C. Lee, Appl. Catal. B: Environ. 199 (2016) 123–133.
[10] F. Dong, Z. Wang, Y. Li, W.K. Ho, S.C. Lee, Environ. Sci. Technol. 48 (2014) 10345–10353.
[11] Y. Huang, Y. Gao, Q. Zhang, Y. Zhang, J.J. Cao, W. Ho, S.C. Lee, J. Hazard. Mater. 354 (2018) 54–62.
[12] Y. Huang, D. Zhu, Q. Zhang, Y. Zhang, J.J. Cao, Z. Shen, W. Ho, S.C. Lee, Appl. Catal. B: Environ. 234 (2018) 70–78.
[13] J. Schneider, M. Matsuoka, M. Takeuchi, J. Zhang, Y. Horiuchi, M. Anpo, D.W. Bahnemann, Chem. Rev. 114 (2014) 9919–9986.
[14] X. Chen, S.S. Mao, Chem. Rev. 107 (2007) 2891–2959.
[15] S. Pu, R. Zhu, H. Ma, D. Deng, X. Pei, F. Qi, W. Chu, Appl. Catal. B: Environ. 218 (2017) 208–219.
[16] A. Martin, A. Sarkar, Nanotoxicology 11 (2017) 713–724.
[17] R.K. Shukla, A. Kumar, D. Gurbani, A.K. Pandey, S. Singh, A. Dhawan, Nanotoxicology 7 (2013) 48–60.
[18] C.M. Sayes, R. Wahi, P.A. Kurian, Y. Liu, J.L. West, K.D. Ausman, D.B. Warheit, V.L. Colvin, Toxicol. Sci. 92 (2006) 174–185.
[19] R.A. Damodar, T. Swaminathan, Chem. Eng. J. 144 (2008) 59–66.
[20] J. Matos, J. Laine, J.M. Herrmann, D. Uzcategui, J.L. Brito, Appl. Catal. B: Environ. 70 (2007) 461–469.
[21] T.H. Xie, J. Lin, J. Phys. Chem. C 111 (2007) 9968–9974.
[22] Y. Ohko, Y. Nakamura, A. Fukuda, S. Matsuzawa, K. Takeuchi, J. Phys. Chem. C 112 (2008) 10502–10508.
[23] A. Šuligoj, U.L. Štangar, A. Ristić, M. Mazaj, D. Verhovšek, N.N. Tušar, Appl. Catal. B: Environ. 184 (2016) 119–131.
[24] J.J. Park, J.G. Lee, D.Y. Kim, J.H. Hong, J.J. Kim, S. Hong, S.S. Yoon, Environ. Sci. Technol. 46 (2012) 12510–12518.
[25] Z. Bian, F. Cao, J. Zhu, H. Li, Environ. Sci. Technol. 49 (2015) 2418–2424.
[26] A. Mukhopadhyay, S. Basak, J.K. Das, S.K. Medda, K. Chattopadhyay, G. De, ACS Appl. Mater. Interface 2 (2010) 2540–2546.
[27] Q. Zhang, C. Sun, Y. Zhao, S. Zhou, X. Hu, P. Chen, Environ. Sci. Technol. 44 (2010) 8270–8275.
[28] A.O. Patrocinio, L.F. Paula, R.M. Paniago, J. Freitag, D.W. Bahnemann, ACS Appl. Mater. Interface 6 (2014) 16859–16866.
[29] S. Banerjee, D.D. Dionysiou, S.C. Pillai, Appl. Catal. B: Environ. 176-177 (2015) 396–428.
[30] K. Liu, M. Cao, A. Fujishima, L. Jiang, Chem. Rev. 114 (2014) 10044–10094.
[31] T. Watanabe, S. Fukayama, M. Miyauchi, A. Fujishima, K. Hashimoto, J. Sol-Gel Sci. Technol. 19 (2000) 71–76.
[32] H.-J. Nam, T. Amemiya, M. Murabayashi, K. Itoh, J. Phys. Chem. B 108 (2004) 8254–8259.
[33] Y. Li, T.J. White, S.H. Lim, J. Solid State Chem. 177 (2004) 1372–1381.
[34] B.L. Bischoff, M.A. Anderson, Chem. Mater. 7 (1995) 1772–1778.
[35] G. Oskam, A. Nellore, R.L. Penn, P.C. Searson, J. Phys. Chem. B 107 (2003) 1734–1738.
[36] H.S. Jung, H. Shin, J.R. Kim, J.Y. Kim, K.S. Hong, J.K. Lee, Langmuir 20 (2004) 11732–11737.
[37] F. Zuo, L. Wang, T. Wu, Z. Zhang, D. Borchardt, P. Feng, J. Am. Chem. Soc. 132 (2010) 11856–11857.
[38] F. Zuo, K. Bozhilov, R.J. Dillon, L. Wang, P. Smith, X. Zhao, C. Bardeen, P. Feng, Angew. Chem. Int. Ed. 51 (2012) 6223–6226.
[39] X. Chen, L. Liu, Y.Y. Peter, S.S. Mao, Science 331 (2011) 746–750.
[40] Y. Chen, W. Li, J. Wang, Y. Gan, L. Liu, M. Ju, Appl. Catal. B: Environ. 191 (2016) 94–105.
[41] J. Su, X. Zou, J.S. Chen, RSC Adv. 4 (2014) 13979–13988.
[42] J. Yu, S. Wang, J. Low, W. Xiao, Phys. Chem. Chem. Phys. 15 (2013) 16883–16890.
[43] Z. Zhao, Y. Sun, F. Dong, Nanoscale 7 (2015) 15–37.
[44] S. Cao, J. Low, J. Yu, M. Jaroniec, Adv. Mater. 27 (2015) 2150–2176.
[45] J. Zhang, Y. Chen, X. Wang, Energy Environ. Sci. 8 (2015) 3092–3108.
[46] F. Ding, D. Yang, Z. Tong, Y. Nan, Y. Wang, X. Zou, Z. Jiang, Environ. Sci.: Nano 4 (2017) 1455–1469.
[47] L. Jiang, X. Yuan, G. Zeng, J. Liang, Z. Wu, H. Wang, Environ. Sci.: Nano 5 (2018) 599–615.
[48] G. Li, Z. Lian, W. Wang, D. Zhang, H. Li, Nano Energy 19 (2016) 446–454.
[49] J. Zhang, M. Zhang, L. Lin, X. Wang, Angew. Chem. Int. Ed. 54 (2015) 6297–6301.
[50] C. Ye, J.-X. Li, Z.J. Li, X.B. Li, X.B. Fan, L.P. Zhang, B. Chen, C.H. Tung, L.Z. Wu, ACS Catal. 5 (2015) 6973–6979.
[51] Y. Zhang, A. Thomas, M. Antonietti, X.C. Wang, J. Am. Chem. Soc. 131 (2009) 50–51.
[52] In: ISO 2409: 2013 Paints and Varnishes — Cross-cut Test.
[53] In: ISO 15989: 2004 Plastics — Film and Sheeting — Measurement of Water-contact Angle of Corona-treated Films.
[54] X. She, H. Xu, Y. Xu, J. Yan, J. Xia, L. Xu, Y. Song, Y. Jiang, Q. Zhang, H. Li, J. Mater. Chem. A 2 (2014) 2563–2570.
[55] X. Dang, X. Zhang, W. Zhang, X. Dong, G. Wang, C. Ma, X. Zhang, H. Ma, M. Xue, RSC Adv. 5 (2015) 15052–15058.
[56] S.C. Yan, Z.S. Li, Z.G. Zou, Langmuir 25 (2009) 10397–10401.
[57] X. Xin, T. Xu, J. Yin, L. Wang, C. Wang, Appl. Catal. B: Environ. 176-177 (2015) 354–362.
[58] G. Liu, L.C. Yin, J. Wang, P. Niu, C. Zhen, Y. Xie, H.M. Cheng, Energy Environ. Sci. 5 (2012) 9603–9610.
[59] D. Vorkapic, T. Matsoukas, J. Am. Ceram. Soc. 81 (1998) 2815–2820.
[60] J.N. Hart, L. Bourgeois, R. Cervini, Y.-B. Cheng, G.P. Simon, L. Spiccia, J. Sol-Gel Sci. Techn. 42 (2007) 107–117.
[61] C. Leyva-Porras, A. Toxqui-Teran, O. Vega-Becerra, M. Miki-Yoshida, M. Rojas-Villalobos, M. García-Guaderrama, J.A. Aguilar-Martínez, J. Alloy. Compd. 647 (2015) 627–636.
[62] K. Qi, J.H. Xin, ACS Appl. Mater. Interface. 2 (2010) 3479–3485.
[63] Y. Chen, B. Wang, S. Lin, Y. Zhang, X. Wang, J. Phys. Chem. C 118 (2014) 29981–29989.
[64] L. Zhang, R. Dillert, D. Bahnemann, M. Vormoor, Energy Environ. Sci. 5 (2012) 7491–7507.
[65] R. Wang, K. Hashimoto, A. Fujishima, M. Chikuni, E. Kojima, A. Kitamura, M. Shimohigoshi, T. Watanabe, Nature 388 (1997) 431.
[66] I. Konstantinou, Appl. Catal. B: Environ. 42 (2003) 319–335.
[67] M. Chen, J. Yao, Y. Huang, H. Gong, W. Chu, Chem. Eng. J. 334 (2018) 453–461.
[68] W.-J. Ong, L.K. Putri, L.-L. Tan, S.-P. Chai, S.-T. Yong, Appl. Catal. B: Environ. 180 (2016) 530–543.
[69] F. Wang, P. Chen, Y. Feng, Z. Xie, Y. Liu, Y. Su, Q. Zhang, Y. Wang, K. Yao, W. Lv, G. Liu, Appl. Catal. B: Environ. 207 (2017) 103–113.
[70] S. Tan, Z. Xing, J. Zhang, Z. Li, X. Wu, J. Cui, J. Kuang, Q. Zhu, W. Zhou, J. Catal. 357 (2018) 90–99.